Geoscience Frontiers 15 (2024) 101816

Contents lists available at ScienceDirect

Geoscience Frontiers

journal homepage: www.elsevier.com/locate/gsf

Research Paper

Pore-scale water–gas distribution and gas permeability of natural gas hydrate reservoirs in the South China Sea

Yuxuan Xia [a], Derek Elsworth [b], Jianchao Cai [a,*], Cheng Lu [c,d], Chao Ma [c]

[a] National Key Laboratory of Petroleum Resources and Engineering, China University of Petroleum, Beijing 102249, China
[b] Department of Energy and Mineral Engineering, G3 Center and Energy Institute, The Pennsylvania State University, University Park 16802, PA, United States
[c] Guangzhou Marine Geological Survey, China Geological Survey, Guangzhou 510075, China
[d] Center of Oil & Natural Gas Resource Exploration, China Geological Survey, Beijing 100083, China

ARTICLE INFO

Article history:
Received 1 December 2023
Revised 11 February 2024
Accepted 29 February 2024
Available online 6 March 2024
Handling Editor: E. Shaji

Keywords:
Natural gas hydrate
Clayey-silt sediments
Gas saturation
Gas permeability
Microstructure

ABSTRACT

Challenges in water drainage within natural gas hydrate reservoirs in the Shenhu area of the South China Sea, characterized by high clay content and strong hydrophilicity, significantly hinder natural gas recovery. Examining the effects of gas pressure and liquid/gas saturation on gas permeability reveals essential insights for increasing gas production potential. We report gas displacement experiments on clayey-silt sediment samples, alongside X-ray computed tomography imaging, that reveal critical findings: a notable increase in flow rate and permeability as displacement pressure nears compaction pressure, highlighting the role of pressure management in enhancing recovery; water displacement from varying pore sizes under different pressures, highlighting the influence of pore size on fluid dynamics, and structural changes, including microfracture formation and a significant fracture that enlarges total pore space by about 15%, which collectively suggest methods to improve gas flow and recovery. Moreover, our analysis identifies average throat length, fractal dimension, and succolarity as principal controls on gas permeability, indicating the substantial impact of microstructural properties on extraction efficiency. These outcomes offer valuable strategies for optimizing natural gas hydrate reservoir development in the South China Sea, emphasizing the need for meticulous pressure and saturation control and in applying a deep understanding of microstructural dynamics.

1. Introduction

Natural gas hydrate, known for its ice-like structure that traps gas molecules within a structural water cage under specific low-temperature and high-pressure conditions, represents a vast, untapped source of energy with the potential to significantly impact global energy strategies (Sloan, 2003; Cui et al., 2018; Esmaeilzadeh et al., 2020; Gajanayake et al., 2023). Predominantly located in shallow marine sediments and permafrost (Waite et al., 2009; Liu et al., 2011; Ruppel and Kessler, 2017; Li et al., 2021), methane hydrates offer a promising alternative to traditional fossil fuels, representing extensive reserves that could meet global energy demands (Makogon et al., 2007; Ning et al., 2020). The Shenhu area of the South China Sea has emerged as a significant site for hydrate exploration, with China's successful extraction trials in 2017 and 2020 marking a milestone in hydrate recovery (Li et al., 2018; Ye et al., 2020). Unlike the sandy textures of hydrate deposits found in regions such as Canada's Mackenzie Delta or Japan's Eastern Nankai Trough (Dallimore et al., 2008; Schoderbek et al., 2012; Yamamoto et al., 2014; Wu et al., 2017), the South China Sea's deposits are encased in unconsolidated clayey-silt sediments, posing unique challenges to extraction and recovery, due to their high clay content and distinct sedimentological characteristics (Yu et al., 2014; Zhang et al., 2017; Li et al., 2018; Dong et al., 2020; Qin et al., 2020).

When recovering the native gas from such clayey-silt reservoirs by depressurization (Sun et al., 2019; Zhao et al., 2020), the decomposition front extends continuously from the wellbore to the interior of the reservoir and the produced gas–water two-phase fluids need to pass through the clayey-silt porous medium in the decomposition zone to be produced (Lu et al., 2023a; Fig. 1). Escape of the dissociated water and hydrate-decomposed water are limited by the low gas permeability and high water-absorbent clay content of the clayey-silt reservoir – resulting in water blocking damage and impeding natural gas production (Chen et al., 2020; Zhang

* Corresponding author.
E-mail address: caijc@cup.edu.cn (J. Cai).

https://doi.org/10.1016/j.gsf.2024.101816

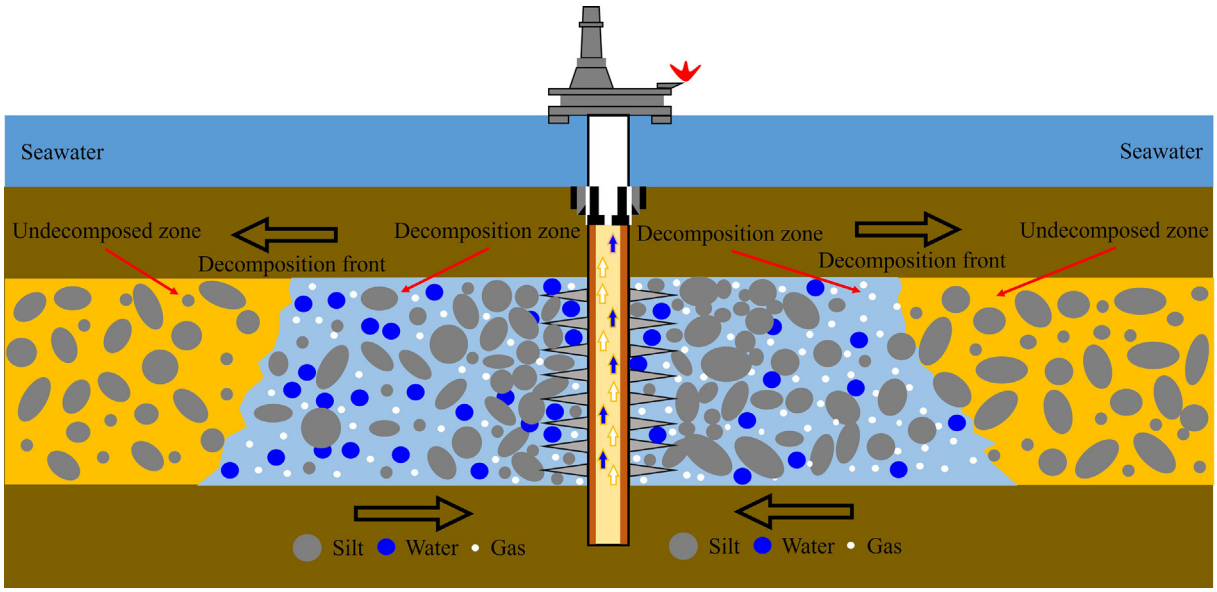

Fig. 1. Schematic diagram of clayey-silt natural gas hydrate reservoir produced by depressurization.

et al., 2022). Meanwhile, dissociation-related structural changes in the substrate fabric and particle migration further reduce permeability and further inhibit gas production (Waite et al., 2004; Boswell et al., 2019). Therefore, sustaining and indeed enhancing gas permeability is one fundamental need in promoting long-term sustained and low-impedance production.

The recovery efficiency from these hydrate reservoirs is critically dependent on understanding and optimizing gas permeability, a complex function of the sediment's porosity, pore-throat architecture, and the physicochemical interactions between the gas and water phases (Ren et al., 2020; Shaibu et al., 2021; Gong et al., 2023). Existing models, including capillary and pore network models, have provided a foundational framework for predicting gas flow through these media. Yet, they often fall short in accurately capturing the real complexities of the sediments, particularly in the diverse conditions presented by the South China Sea's clayey-silt compositions (Dai and Seol, 2014; Katagiri et al., 2017; Chen et al., 2018; Cai et al., 2020b). This discrepancy highlights a significant research gap, underscoring the need for empirical studies that can ground-truth theoretical models against real-world data. Furthermore, the technical and logistical challenges associated with conducting in-situ permeability and multiphase flow measurements further complicate our understanding of these systems, making it difficult to predict and effectively enhance recovery outcomes (Minagawa et al., 2008; Konno et al., 2013; Delli and Grozic, 2014; Yoneda et al., 2019).

To address these shortcomings, this study completes a series of gas displacement experiments using water-saturated clayey-silt samples from the South China Sea under variable gas pressures. Employing a novel experimental setup that integrates gas flow measurement with X-ray computed tomographic (CT) imaging (Lu et al., 2019; Cai et al., 2020a), the study aims to dissect the intricate relationships among gas pressure, water saturation, and permeability within these unique sedimentary environments. By meticulously analyzing the response of dissociated hydrate sediments and their permeability evolution, this research seeks to unravel the critical factors that govern gas recovery efficiency. Such insights are pivotal in refining predictive models and developing more effective strategies for hydrate gas extraction, particularly within the challenging contexts presented by clayey-silt reservoirs.

2. Natural gas hydrate reservoir samples

The samples are obtained from the gas hydrate reservoir test well in the Shenhu area, South China Sea. The reservoir is located in the Baiyun Sag of the Pearl River Mouth Basin at a depth of ~1495–1545 m. The reservoir comprises unconsolidated clayey silt with a mean median particle size of 12 μm. The average effective porosity of the reservoir is 34% with an average hydrate saturation of 32.5% (Li et al., 2018). The pressurized sample is recovered by in situ sampling from the seabed and is used in this work after the release of natural gas by depressurization (Fig. 2).

Previous studies have defined sample pore structure, mineral composition, and wetting characteristics by scanning electron microscope, quantitative evaluation of minerals by scanning electron microscopy, and sessile drop methods (Lu et al., 2022). The combined micro- and nano-scale porosity is ~20%, with a median pore radius of only ~0.1 μm in the low permeability sediments. The sample comprises mainly quartz and feldspar (~50%), carbonate (~15%) and a relatively high content of clay minerals (20%–30%) – predominantly water-absorbent illite (greater than 70%). The mean contact angle is ~50°, identifying strong hydrophilic characteristics, making the reservoir prone to water block. We specifically investigate the feature and its impact on gas-phase flow and permeability.

This work conducts single-phase water flow experiments on the sample and obtain the permeability evolution characteristics caused by structural changes (Lu et al., 2019; Cai et al., 2020a). The sample exhibits the highest permeability at an upstream pressure of 30 kPa (equivalent to 3 MPa/m within the sample). Further increasing the pressure led to a significant reduction in permeability, attributed to structural creep and the resultant narrowing of pores and throats in the sample, and emphasizing the importance of structural evolution in controlling permeability.

3. Experimental procedures

Gas is injected into the water-saturated sample at incremented pressures and the gas saturation allowed to stabilize. The permeability is then measured at this particular gas saturation and the gas–water distribution is obtained by X-ray CT imaging – before the pressure is incremented and the procedure repeated.

Fig. 2. Clayey-silt sediment sample.

The gas permeability of the sample is measured using non-sorbing nitrogen gas. A steady pressure differential is maintained between upstream to downstream and the outlet flow rate recorded. The gas permeability is measured assuming steady isothermal flow as:

$$K_g = \frac{2Q_0 p_0 \mu L}{A(p_1^2 - p_2^2)} \quad (1)$$

where K_g is the gas permeability, p_0 is atmospheric pressure, A is the cross-sectional area of the sample, μ is the gas viscosity, L is the length of the sample, and p_1 and p_2 are the absolute pressures at the inlet and outlet, respectively.

3.1. Apparatus

We use a special non-magnetic sample holder and micro-CT system to obtain the pore-scale distribution of the individual two-phase fluids during the permeability measurement. The gas seepage apparatus includes a gas source, pressure regulator, gas flowmeter and electronic balance (Fig. 3). The special non-magnetic and X-ray transparent sample holder is fabricated from polyimide – with high strength, thermal stability, limited optical transparency and full X-ray transparency. The micro-CT system consists of a micro-CT scanner and a data reconstruction and processing system. This performs high resolution scanning of the sam-

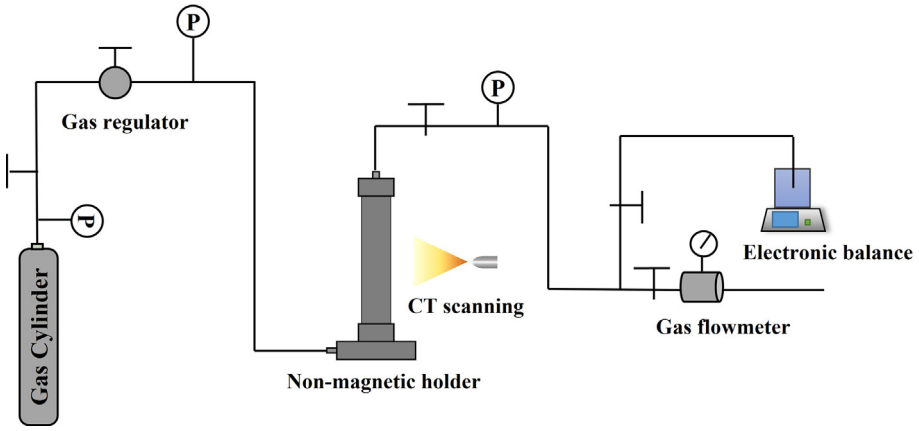

Fig. 3. Schematic diagram of experimental setup.

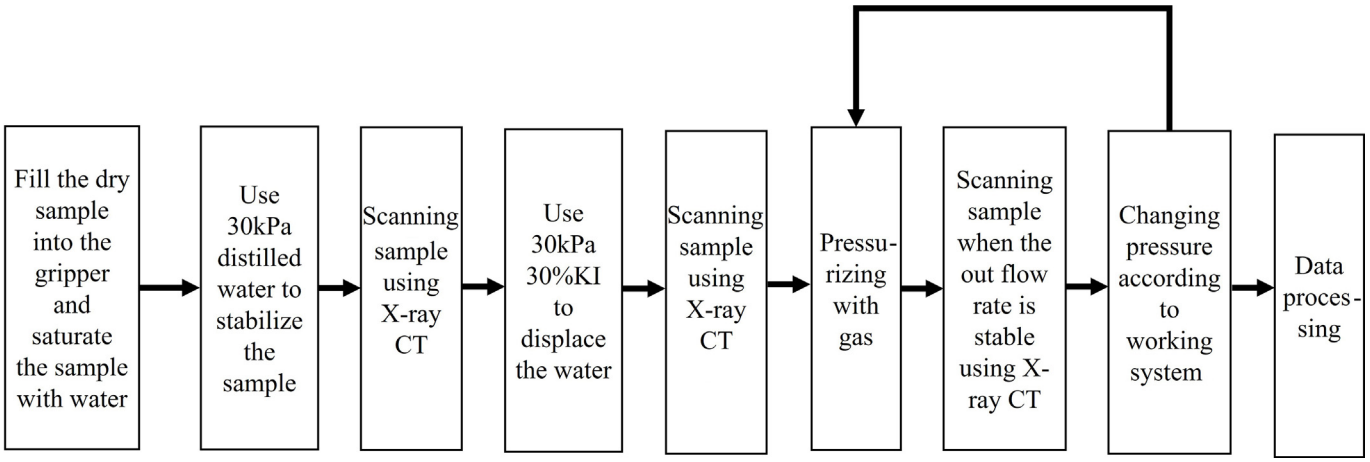

Fig. 4. Experimental sequence for the gas displacement experiment.

ple in the X-ray transparent core-holder at micrometer resolution to obtain the complete three-dimensional grain-pore structure and multiphase fluid distribution within the pores.

3.2. Procedures

The following experimental procedure is followed.

Table 1
Gas flow rate and permeability under different up- and down-stream pressures.

Gas displacement pressures (kPa)		Upstream pressure (kPa)	Downstream pressure (kPa)	Flow rate (mL/min)	Permeability (mD)
10		9.2	0	0.11	0.6951
20		21	0.5	7.11	19.0647
30		29.9	0.2	33	58.8324
40	40	41.5	0.6	99	121.9161
	30	30	0.4	73	130.417
	20	20.3	0.3	50	137.972
	10	10.5	0.1	27	149.9552
50	50	52.2	0.7	124	116.1746
	40	39.8	0.6	96	124.2066
	30	30.1	0.4	74	131.2023
	20	19.8	0.3	50	141.8255
	10	10.4	0.2	28	158.5583
75	75	75.8	0.1	173	102.0959
	50	49.5	0.7	119	118.9084
	40	40	0.6	96	123.4751
	30	29.4	0.4	72	131.6288
	20	19.4	0.4	49	142.1535
	10	9.9	0.1	26	153.6718
100	100	101.3	1.3	215	86.9215
	75	75.3	1	167	99.3952
	50	50.3	0.7	118	115.6434
	40	39.2	0.6	94	123.8134
	30	30.6	0.4	74	129.7308
	20	20.3	0.3	51	140.7315
	10	9.9	0.1	26	153.6718

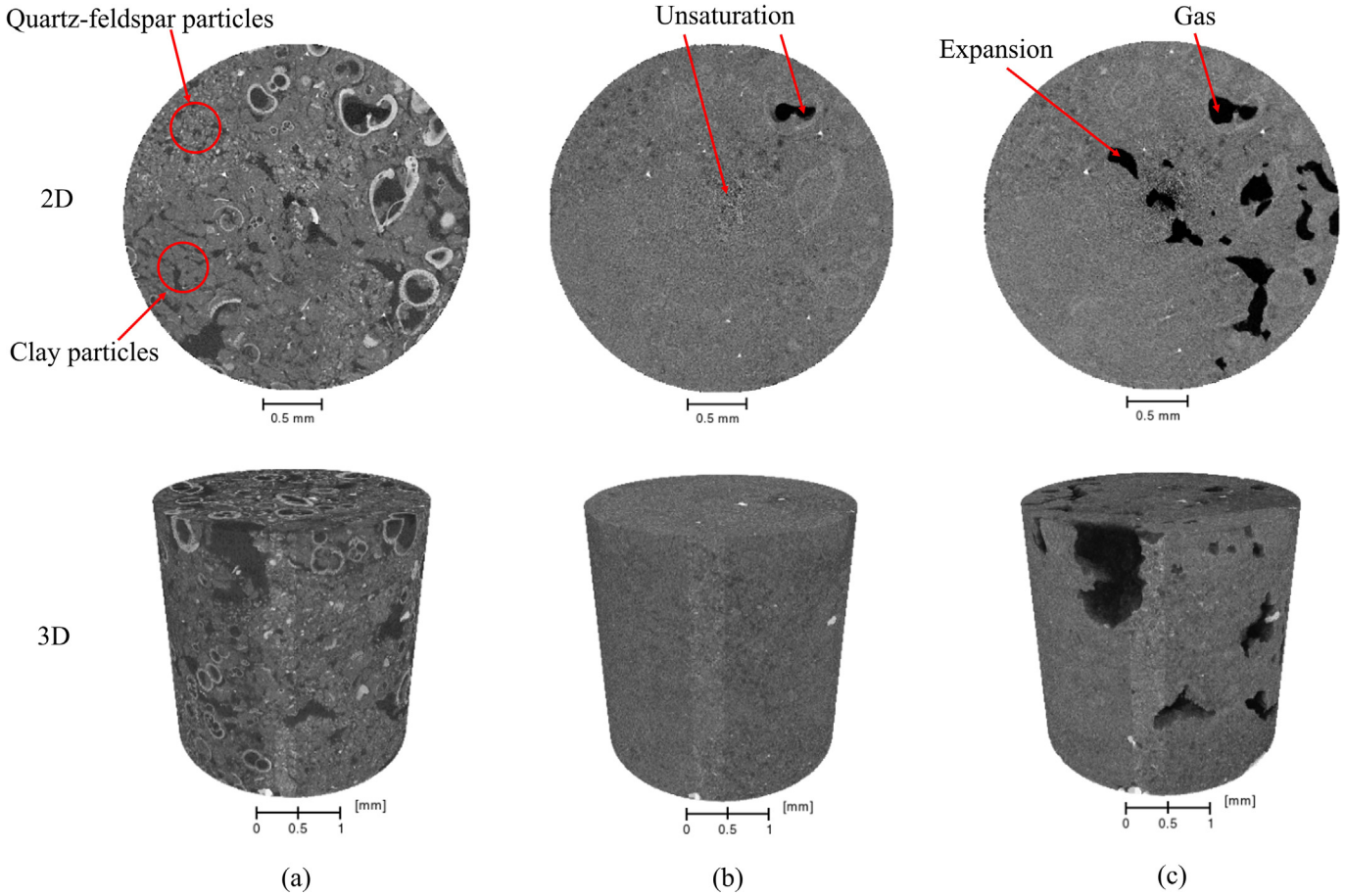

Fig. 5. 2D and 3D grayscale images of the sample under different experimental conditions. (a) 30 kPa water, (b) 30 kPa 30% KI, (c) 10 kPa gas.

(1) The clayey-silt sample is first dried then mounted in the core-holder (8 mm in diameter and 10 mm in length). Distilled water is added during the filling process to render the sample 100% water saturated as the core-holder is completely filled.

(2) The sample is compacted/consolidated under a constant pressure and pressure gradient along the sample for 24 h before a permeability measurement is made. An upstream pressure of 30 kPa (corresponding to a pressure gradient of 3 MPa/m) is selected to effectively stabilize the clayey-silt sample (Lu et al., 2019) – representing a compromise to provide suitable consolidation but to not significantly activate transient creep. The X-ray CT imaging is performed (at a resolution of 2.4557 μm per voxel) when the outlet flow rate is stable – this defines the original structure of the sample prior to the gas displacement experiment.

(3) 30% potassium iodide (KI)-water solution is displaced into the sample at a constant pressure of 30 kPa to add contrast and aid later image processing to obtain the water distribution. Imaging is conducted once the flow rate of the KI-water solution at the outlet is stable.

(4) Upstream gas pressures of 10, 20, 30, 40, 50, 75, and 100 kPa are then applied for the nitrogen gas displacement – with each stable flow imaged by X-ray CT for 10, 20, 30 and 50 kPa.

(5) Experimental data and CT images are processed to obtain the gas permeability, gas and water saturation and their distribution in the samples under the various pressure states (Fig. 4).

4. Results and discussion

4.1. Gas flow rate and permeability

Table 1 shows the flow rates and permeabilities of the sample at different up- and down-stream pressures after initial compaction at a pressure of 30 kPa. When gas displacement is initiated with an upstream pressure of ~10 kPa (there is a slight discrepancy in the actual upstream–downstream pressure difference due to equipment precision, which ~9.2 kPa), minimal flow results. With an increase in upstream pressure to 20 kPa, there is a significant increase in flow rate of ~ 70-fold increase. With a further increase in upstream pressure to 30 kPa, the flow rate continues to significantly increase, but now only ~ 5-fold. When the upstream pressure is raised to 40 kPa and exceeds the pre-consolidation pressure of 30 kPa, the flow rate increases a further ~ 3-fold, and we observe a noticeable structural change in the sample from the outer wall of the holder. Additionally, we also observe a slight sanding at the equipment outlet. Due to the small pore size of the clayey-silt samples, the gas slippage effect (wherein the gas permeability is lower at high pressures for the same sample and the same gas) cannot be ignored. After using pressures greater than 30 kPa for gas displacement, the pressure is stepwise decreased to 10 kPa to again measure post-fracturing permeability. Pressures are then further increased to 50, 75 kPa, then 100 kPa, where the sample exhibited consistent flow rates at the same pressure differential. This indicates that starting from 40 kPa, the internal structure and gas–water distribution within the sample had already stabilized and ceased to change. Therefore, CT scans are performed only at 50 kPa as representative for the gas displacement pressures spanning 40 to 100 kPa.

Permeability is obtained from the up- and down-stream gas pressures and measured gas outlet flow rates using Darcy's law for compressible flow Eq. (1). The change in permeability under different gas displacement pressures follows a similar pattern to the flow rate. At a gas displacement pressure of 10 kPa, the permeability only exhibits a minimal increase. However, as the gas displacement pressure increases to 20 kPa, the permeability significantly increases, by a factor of ~27 ×. As the gas displace-

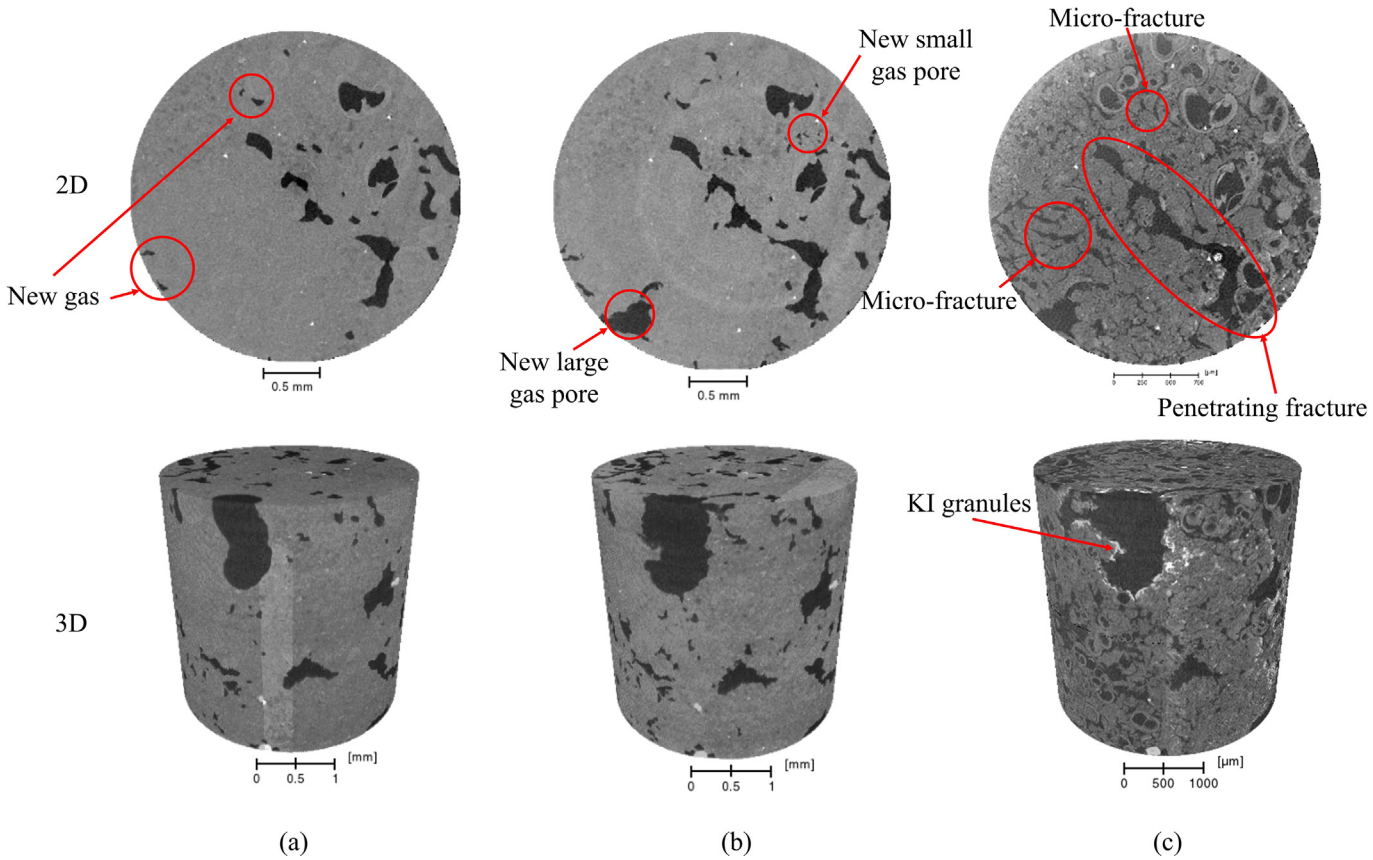

Fig. 6. 2D and 3D grayscale images of the sample under different experimental conditions. (a) 20 kPa gas, (b) 30 kPa gas, (c) 50 kPa gas.

ment pressure further increases to 30 kPa, the permeability continues to exhibit a significant increase, approximately tripling. When the gas displacement pressure reaches 40 kPa, the permeability increases by ~2 × and remains unchanged at progressively higher pressures (albeit when neglecting the gas slippage effect).

4.2. Evolution of pore/grain structure and gas–water distribution

The 2D and 3D grayscale images of the sample under different experimental conditions are shown in Figs. 5 and 6. At 30 kPa there are regions in the sample with larger, poorly sorted quartz and feldspar particles, as well as regions with smaller, well-sorted clay particles. Pores within the sample (pores shown in black) over various pressures are distributed over multiple scales, including macropores distributed between particles and in foraminifera (black pore with white ring) together with small pores distributed among the clay minerals.

Apparent in the 30 kPa image doped with 30% KI-water solution is that the sample is highly water saturated and only a small portion of the foraminifera pores and extremely small pores remain gas saturated due to capillary pressure - causing a small amount of gas to be trapped in the pores. From the images at the reduced pressure of 10 kPa, the KI-water solution is primarily displaced from the larger pores. A significant portion of the KI-water solution in the larger pores is near-completely displaced, with the edges of the pores smoothed by relic water and some pores dilated. At 20 kPa the structure and saturation are similar to at 10 kPa, but now the KI-water solution is also partly displaced from the smaller pores. This continues to 30 kPa but with the addition that KI-water solution is further displaced from a few of the larger pores. It is usually expected that the smaller capillary forces in larger pores (Lu et al., 2023b) will result in them draining first. However, this observed out-of-sequence displacement of fluids from large pores requiring large pressures likely results from the connected pathways containing narrow throats. Furthermore, even as the gas displacement pressure reaches the initial consolidation pressure (30 kPa) some residual water saturation remains. This may also be due to the presence of smaller pore and throat radii requiring a large capillary overpressure to displace the KI-water solution.

As the gas displacement pressure is further increased to 40, 50, 75, and 100 kPa the permeability remains unchanged – suggesting that the gas–water distribution and structure within the sample also remain unchanged. Thus, the X-ray CT image captured at 50 kPa may be considered representative. As shown in Fig. 6, the KI-water solution in the sample has been mostly displaced, and KI particles (bright spots) have precipitated along the edges of some pores. Additionally, the sample has undergone significant particle migration. Compared to the stable sample at 30 kPa, many microfractures connect the intergranular pores and a penetrating fracture cuts the sample from the center to one edge. The appearance of these fractures is the primary reason for the complete displacement of the KI-water solution. In theory, the gas displacement pressure at 50 kPa may struggle to overcome the capillary forces in the micro-scale pores. However, due to the loose and unconsolidated nature of the clayey silt sample, particle migration occurs once the gas displacement pressure exceeds the initial consolidation pressure. This results in the gas creating numerous small fractures and penetrating larger fractures within the sample, enhancing the connectivity of the pores and increasing the throat radii that connect them. As a result, water in the sample is rapidly

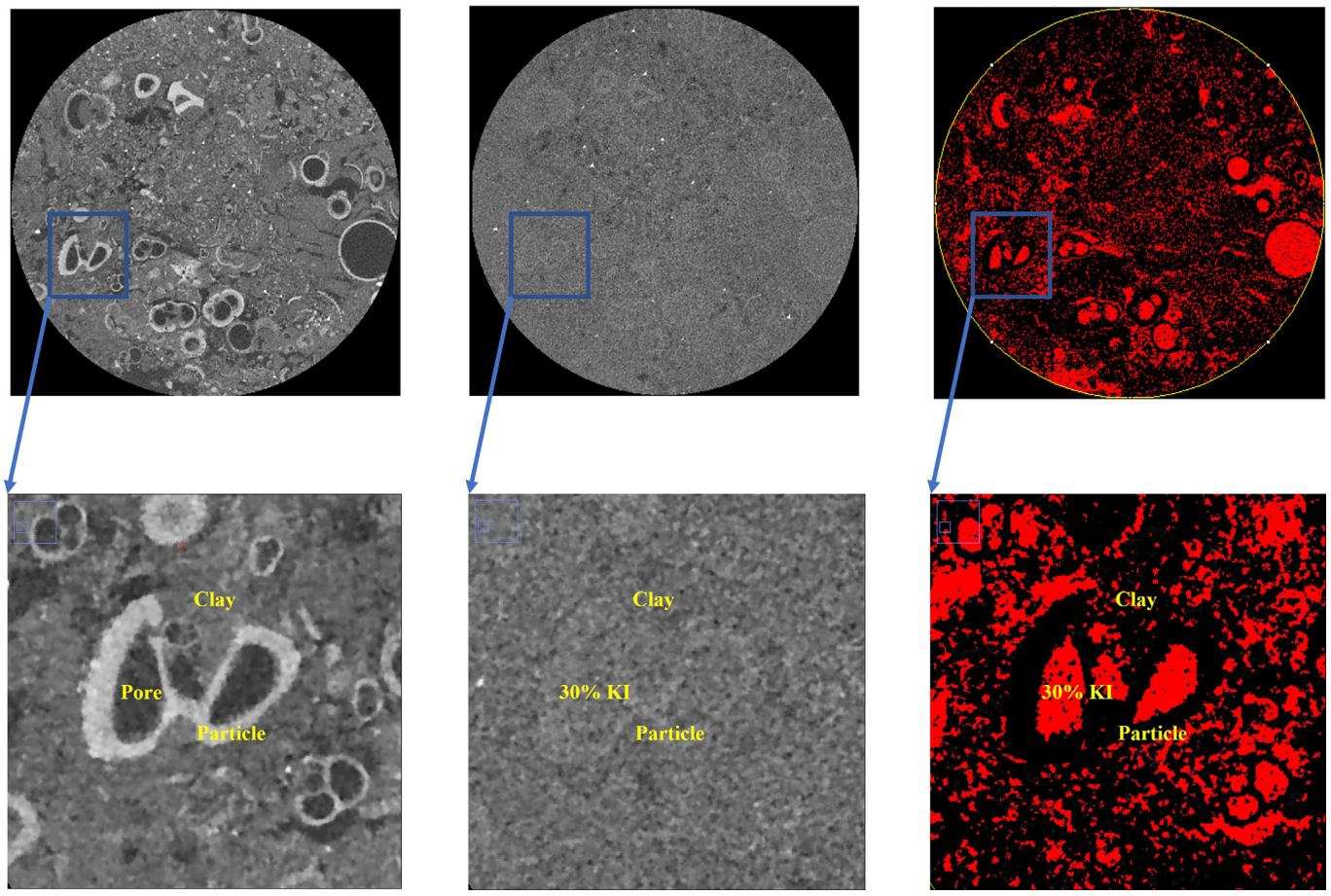

Fig. 7. Image differencing to distinguish among the components of the X-ray CT grayscale image of the sample.

displaced. The pore volume of the post-experiment sample is greater than the initial pore volume.

4.3. Gas-water saturation

Images are processed by cropping, alignment, smoothing and region selection to define the spatial positions of pores and grains within the CT scanned sample at different pressures. Image differencing is used to obtain changes in the pore space and water–gas distributions. The gray value distribution of the image reconstructed by CT imaging is related to the density and atomic number of the fluid and mineral components comprising the sample. The greater the density and the greater the atomic number, the greater the gray value. The 30% doped KI-water solution elevates the atomic number and improved image contrast and therefore resolution. Initially the pores are unsaturated, resulting in a relatively small gray value – manifest as black on the image – delimiting the region where the gas phase is present. The sample image containing KI-water solution and scanned in situ under different pressures is subtracted from the initial sample image – this differenced image defines the pore space containing 30% KI. The presence of the gas phase and grains can also be distinguished by the differencing process (Fig. 7).

The pore space and gas–water distributions within the sample under different pressures are similarly obtained by this image differencing method. Based on the digital core image after binary segmentation, the proportion of voxels in the entire sample is counted to determine the volume proportion of gas and water under different pressures. According to the three-dimensional gas–water distribution images at low gas pressure (10 kPa) (Fig. 8, blue represents water phase and red represents gas phase), the water in the large pores is first displaced. Further increasing the pressure allows the water in the small pores to then be displaced. Finally, when the pressure is increased to 50 kPa, the pore morphology changes significantly – resulting in elongated or fracture-like pores.

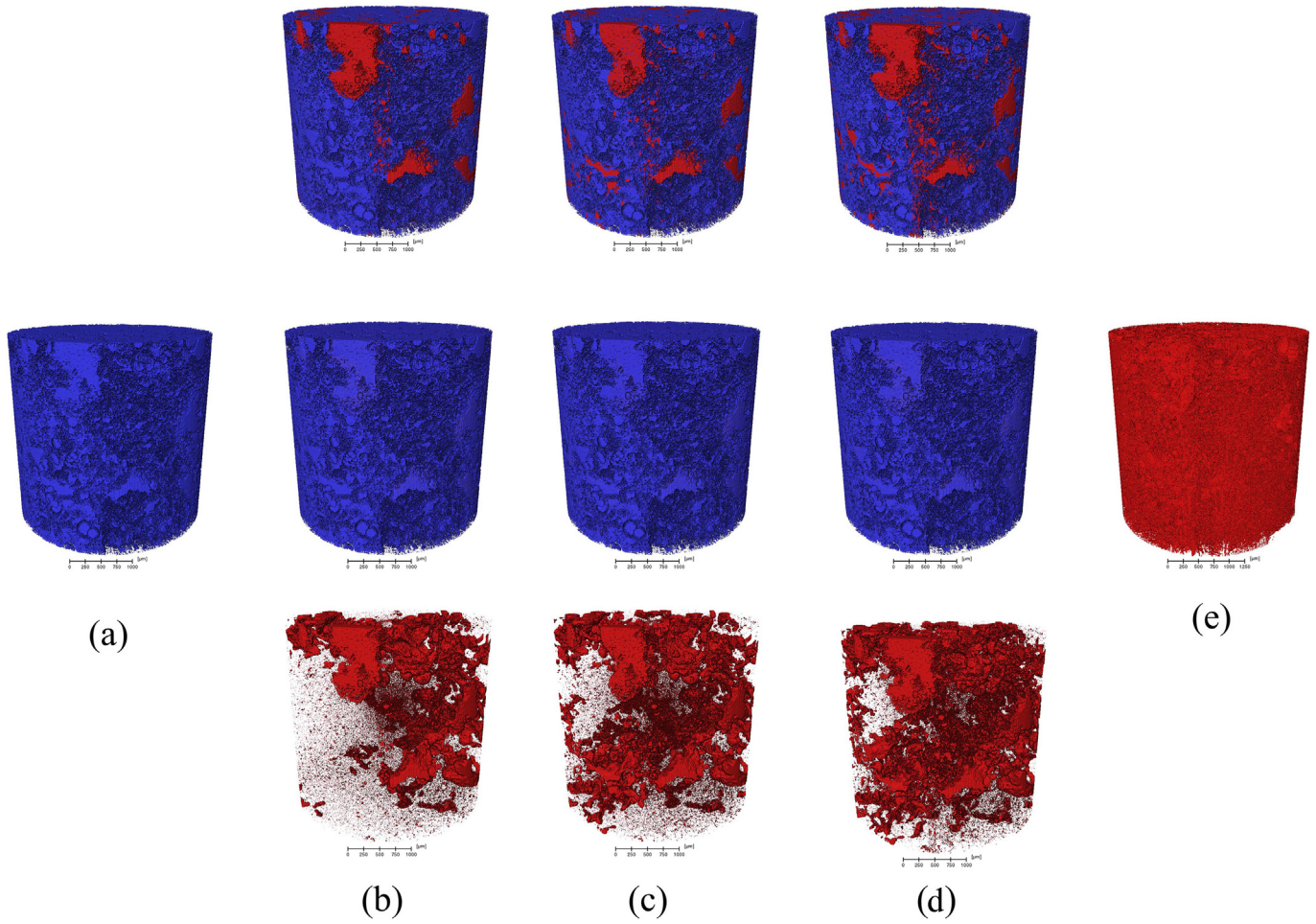

Fig. 8. Pore-scale gas–water distribution after segmentation processing. (a) 30 kPa 30% KI, (b) 10 kPa gas, (c) 20 kPa gas, (d) 30 kPa gas, (e) 50 kPa gas (blue is water phase, red is gas phase). (For interpretation of the references to colour in this figure legend, the reader is referred to the web version of this article.)

Table 2
Gas-water saturation under different pressures and for different fluids.

Experimental conditions		30 kPa 30% KI	10 kPa gas	20 kPa gas	30 kPa gas	50 kPa gas
Gas	Proportion, %	1.42	4.19	5.44	6.47	29.76
	Saturation, %	5.4	15.9	20.6	24.5	98.1
Water	Proportion, %	24.94	22.17	20.92	19.89	0.58
	Saturation, %	94.6	84.1	79.4	75.5	1.9

Table 2 shows the proportion and saturation of gas and water directly calculated from Fig. 8. After saturating at 30 kPa with a 30% KI-water solution, the sample is essentially completely saturated, reaching a liquid saturation of 94.6%. Then, after gas displacement 10 kPa, ~10% of the KI-water solution is displaced, and the gas saturation reaches 15.9%. As the gas displacement pressure increases to 20 kPa then 30 kPa, ~4.7% and ~ 3.9% of the KI-water solution is further displaced, respectively, resulting in a final gas saturation of 24.5%. At this point, there is still 75.5% of the KI-water solution remaining in the sample that has not been displaced. With a further increase in gas displacement pressure, the gas saturation abruptly rises to 98.1%, leaving only 1.9% of the KI-water solution undisplaced. The combined gas–water pore space ratio within the sample after high-pressure displacement increased from 26.36% to 30.34% - an approximately 15% increase.

The two-dimensional vertical slice showcases the heterogeneous distribution of the KI-water solution (Fig. 9), with the direction of displacement oriented against gravity, as depicted in Fig. 10, to lessen gravity's effect. As shown in Fig. 9, the distribution of the KI-water solution saturation demonstrates the pronounced hetero-

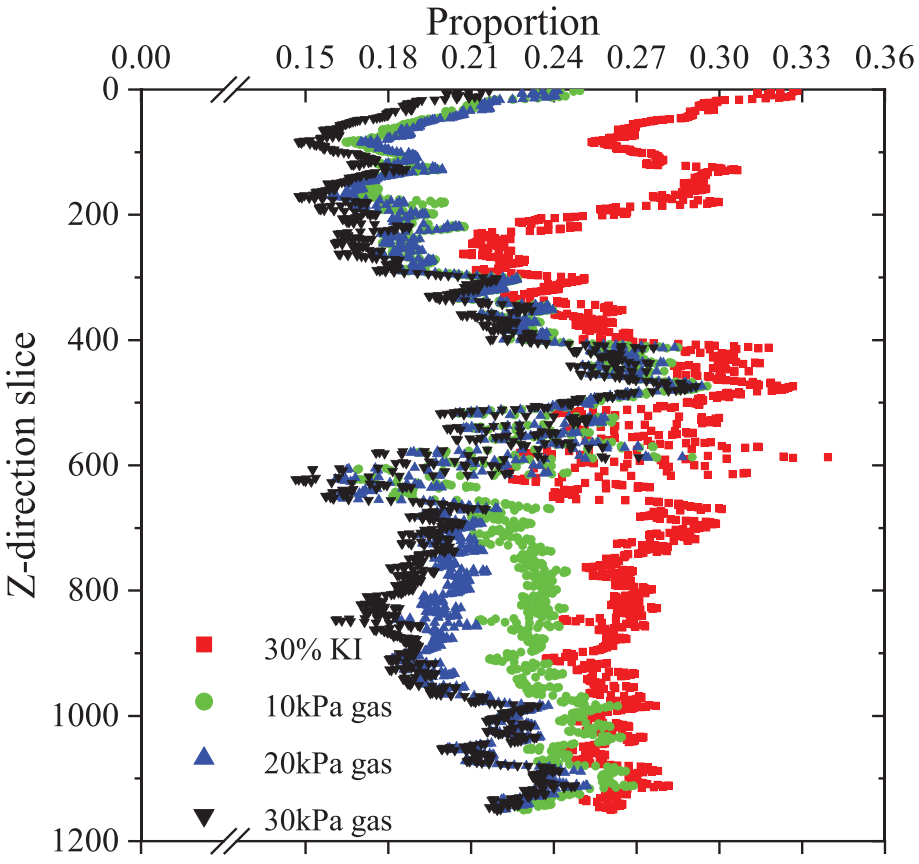

Fig. 9. The heterogeneous distribution of the KI solution in a two-dimensional vertical slice.

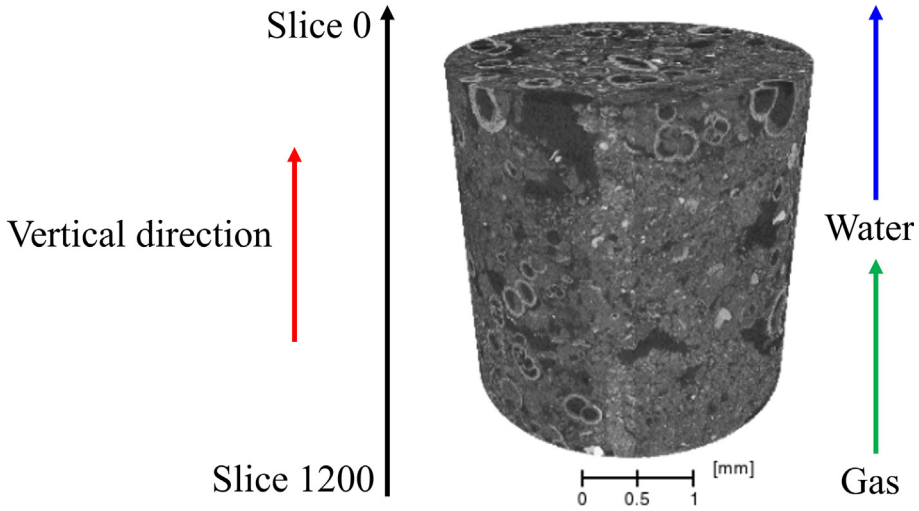

Fig. 10. Fluid displacement direction slice identification in the vertical direction.

geneity that evolves with vertical elevation within the sample. There is a noticeable porosity trough between slices 200 and 300. Comparing the distribution of KI-water solution after 10 kPa gas displacement, it is evident that the liquid saturation remains heterogenous. The displacement primarily occurs upstream (slices 600–900) and then downstream (slices 0–200). That less liquid is displaced from the pores in the center of the sample may be attributed to the narrower throats and lower connectivity in this region. As the gas displacement pressure increases further to 20 kPa and 30 kPa, more liquid is displaced upstream (slices 600–900) with little change downstream (slices 0–200) – possibly since the downstream pores have already been largely desaturated. The liquid in the pores in the center of the sample still experiences minimal changes.

The heterogeneous distribution of gas in a two-dimensional vertical slice is shown in Fig. 11b, with Fig. 11a showing an enlargement for 10–30 kPa. Since there was little change in the pore space after gas displacement at 10–30 kPa, the heterogeneous distribution of gas increase corresponds to the liquid decrease. However, when the gas displacement pressure reached 50 kPa, there is a significant increase in gas content in all slices due to the appearance of fractures. Fig. 12 shows the heterogeneous distribution of pore space in a vertical two-dimensional slice first before and then after displacement. The evolution of pore space is similar to that for the liquid change and identifies the well-connected pores where gas and water readily exchange and are more likely to elongate or fracture. The heterogeneity of the pore space not only controls the distribution of the liquid but also affects the appearance of fractures. The proportion of pore increases significantly in the downstream (slices 0–30) resulting as some particles are expelled from the core holder and indicate the importance of wellbore sand control in exploitation of natural gas hydrate reservoirs.

The change in permeability with gas saturation is shown as Fig. 13 (the gas permeability at 30 kPa is selected for comparison at each gas displacement pressure to eliminate the influence of gas slippage). The water saturation has a significant influence on the gas permeability of the reservoir with a slightly higher water saturation greatly reducing the gas permeability. The displacement by gas does not cause creep in the pore space as for the water saturated case (Lu et al., 2019; Cai et al., 2020a). The gas quickly breaks through the fractures as gas migration and the gas permeability of the reservoir does not change significantly after breakthrough.

4.4. Differing reservoir and laboratory conditions

We complete gas displacing water experiments on clayey silt samples. As the sample is loose and unconsolidated, it is not possible to apply vertical confining pressure in the direction of fluid flow during the experiment, which results in the experimental pressures being much lower than reservoir pressures (~13.5 MPa) (Bian et al., 2023). Similarly, the sample is completely dissociated of hydrates. In situ solid hydrates significantly influence the mechanical properties and structural evolution of the reservoir and impact the distribution of pore space among gas liquid and solid (mineral and hydrate).

However, the primary focus of this study is on the evolution of gas permeability within the gas decomposition zone surrounding the wellbore. In this region, the pressure is relatively low, the hydrates have already fully dissociated, and the structure is loose and prone to evolution. Not only is there decomposed gas, but also a significant amount of free gas flows through this zone into the wellbore. In comparison, the water content is relatively low, with some water trapped in clay pores, resulting in lower water production during exploitation. These conditions are similar to our experimental conditions and thus the results are representative of this state. This decomposition zone around the wellbore is a critical transit zone that potentially rate-limits actual reservoir production

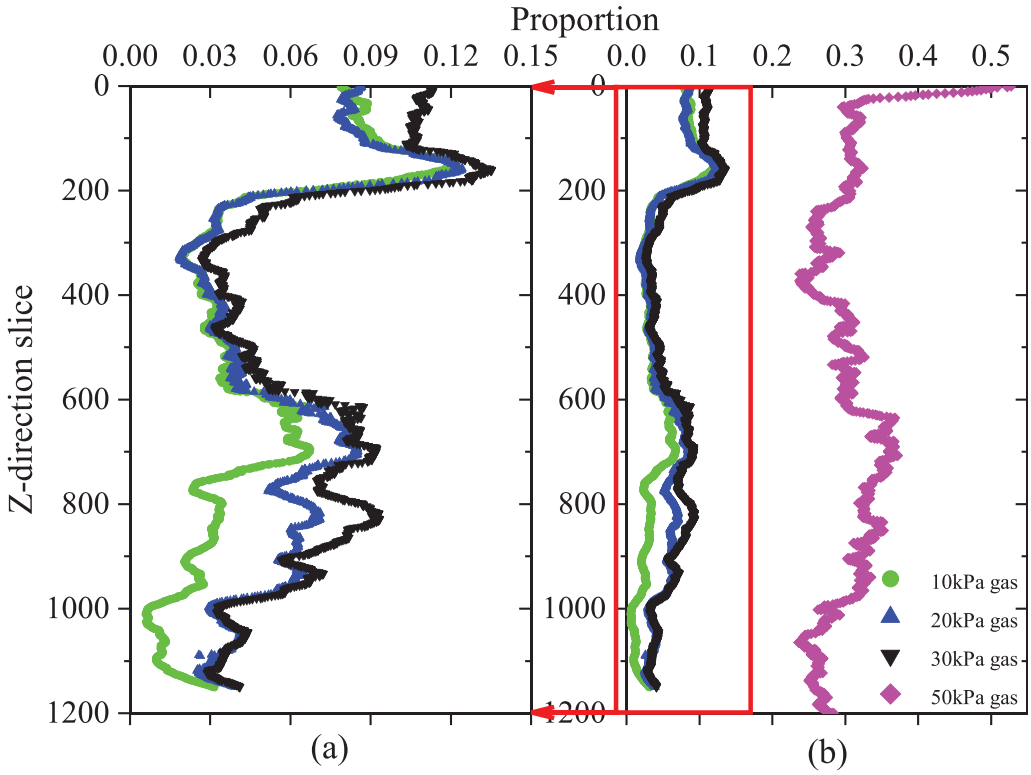

Fig. 11. The heterogeneous distribution of gas in the vertical two-dimensional slices. (a) 10–30 kPa, (b) 10–30 kPa and 50 kPa.

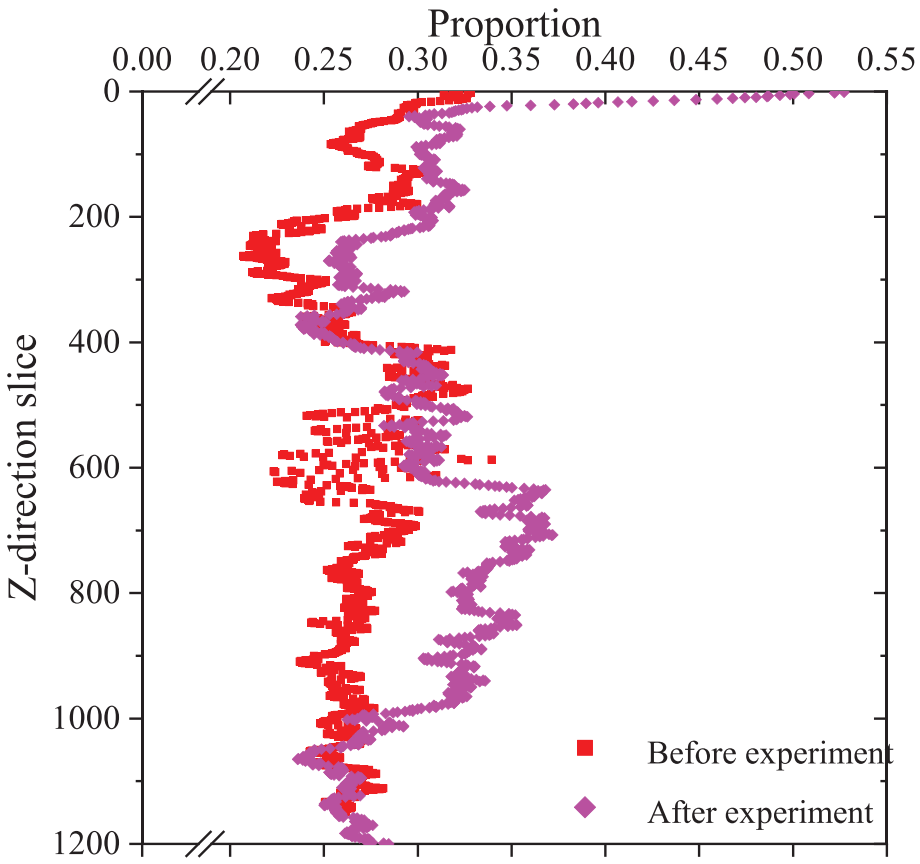

Fig. 12. Heterogeneous distribution of pore space in the vertical two-dimensional slices.

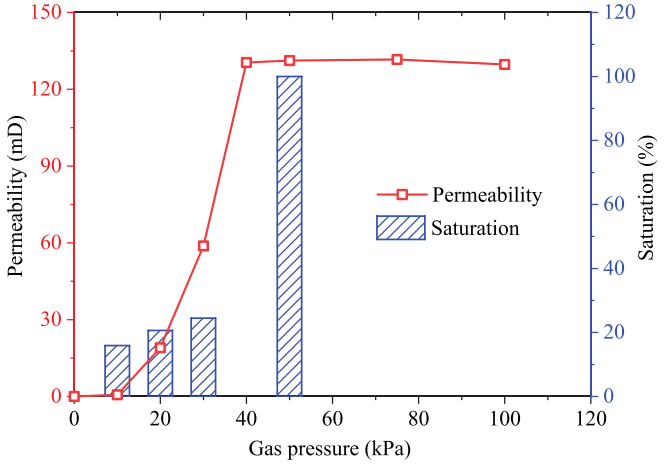

Fig. 13. Gas saturation versus permeability at different gas pressures within the clayey-silt sample.

– and therefore is of significant importance in defining the efficiency of natural gas hydrate recovery.

4.5. Pore network model of gas space

Pore network models (Dong and Blunt, 2009; Blunt et al., 2013) are constructed from the X-ray CT reconstructions (Fig. 8) to represent the gas-filled pore space as shown in Fig. 14. For computational tractability, the structural data from the central 512^3 pixels of the original data volume are selected for calculation. This enables the pore structure parameters for the pore space open to gas flow under different gas pressures to be calculated (Table 3). After displacement with an initial gas pressure of 10 kPa the water in the large pores in the center of the sample is driven out. However, at this time, there are only a few connected pore channels within the sample, resulting in a low relative gas permeability. As the gas displacement pressure is increased to 20 kPa, the gas-filled large pores in the center of the sample gradually extend to the periphery, forming a contiguous gas seepage channel that extends across the sample - the corresponding permeability increases significantly. When the pressure is further increased to 30 kPa, only the water in some small pores is displaced, with the saturation and configuration of the desaturated large pores changing little but with permeability increasing three-fold. When the pressure exceeds the compaction pressure of 30 kPa and reaches 50 kPa, the sample pore space is completely reconstructed by gas-fracturing, forming a number of connected gas flow channels with the permeability further doubling over that at 30 kPa.

The modeled pore throat distribution of the gas seepage channels within the sample under different pressures (Fig. 15) are calculated from the pore network models. Comparing the gas phase volume fraction of pores upon incrementing upstream pressures from 10 to 30 kPa (Fig. 15a), shows that the water in pores with diameters in the range 20–60 μm is expelled and drains. Meanwhile, the displacement of water in transiting from 10 to 20 kPa is larger than that in transiting from 20 to 30 kPa, which are 41% and 12% respectively. The gas phase volume fraction change for the throats in transiting from 10 to 30 kPa (Fig. 15b) shows that with the increase in the gas pressure, the water in pore throats with diameters in the range 10 to 50 μm are mainly driven out.

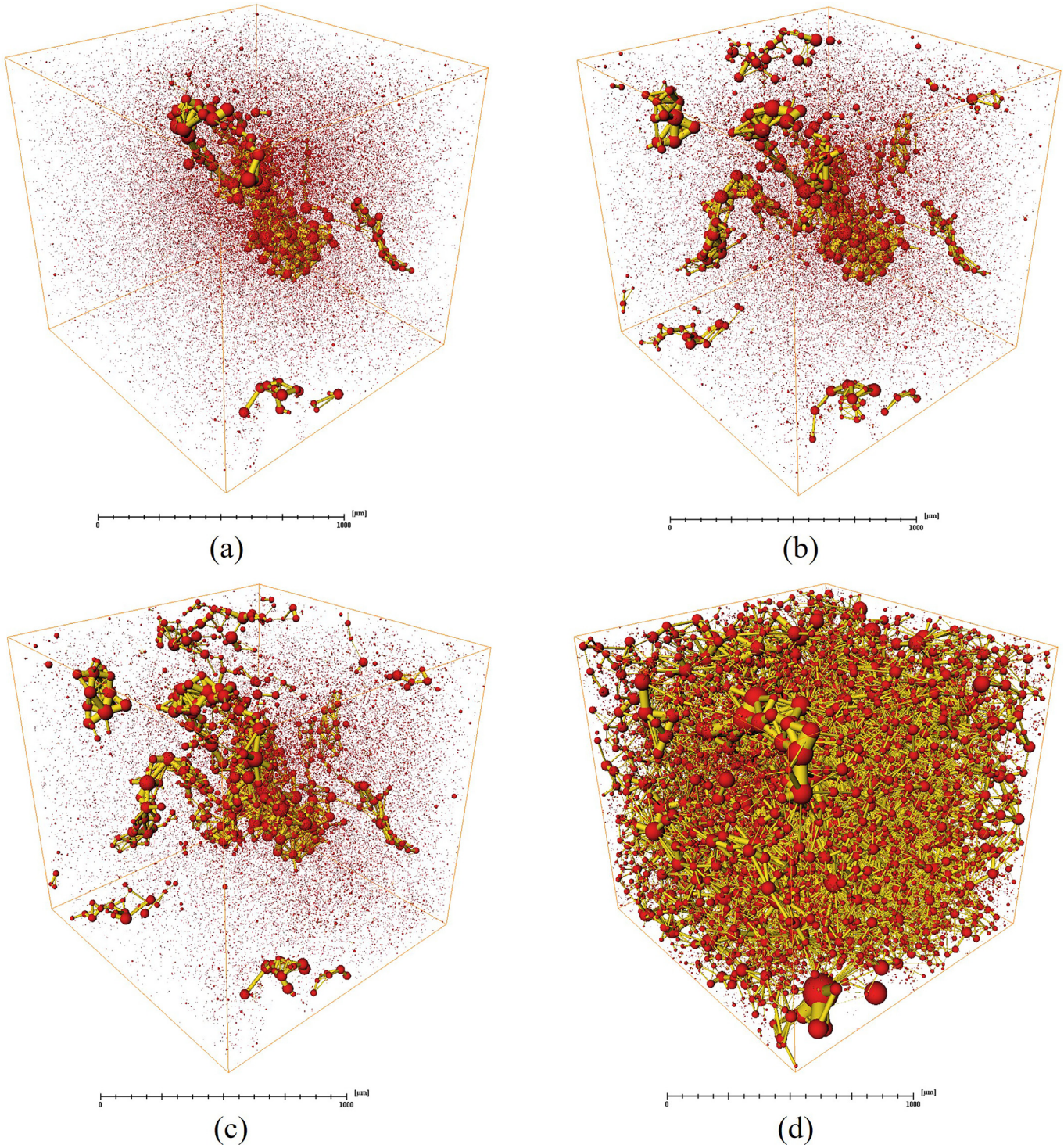

Fig. 14. Pore network models for gas seepage space at different gas displacement pressures. (a) 10 kPa gas, (b) 20 kPa gas, (c) 30 kPa gas, (d) 50 kPa gas.

Table 3
Gas-phase pore-throat structure parameters under different pressures.

Gas displacement pressures (kPa)	Average pore radius (μm)	Maximum pore radius (μm)	Average throat radius (μm)	Maximum throat radius (μm)	Average throat length (μm)	Maximum throat length (μm)	Coordination number
10	2.61	82.71	7.32	73.98	26.97	198.69	0.07
20	2.84	74.94	9.16	73.73	31.50	184.10	0.11
30	2.98	78.13	11.86	79.67	43.94	239.72	0.13
50	6.12	206.64	7.31	134.44	63.19	548.50	1.42

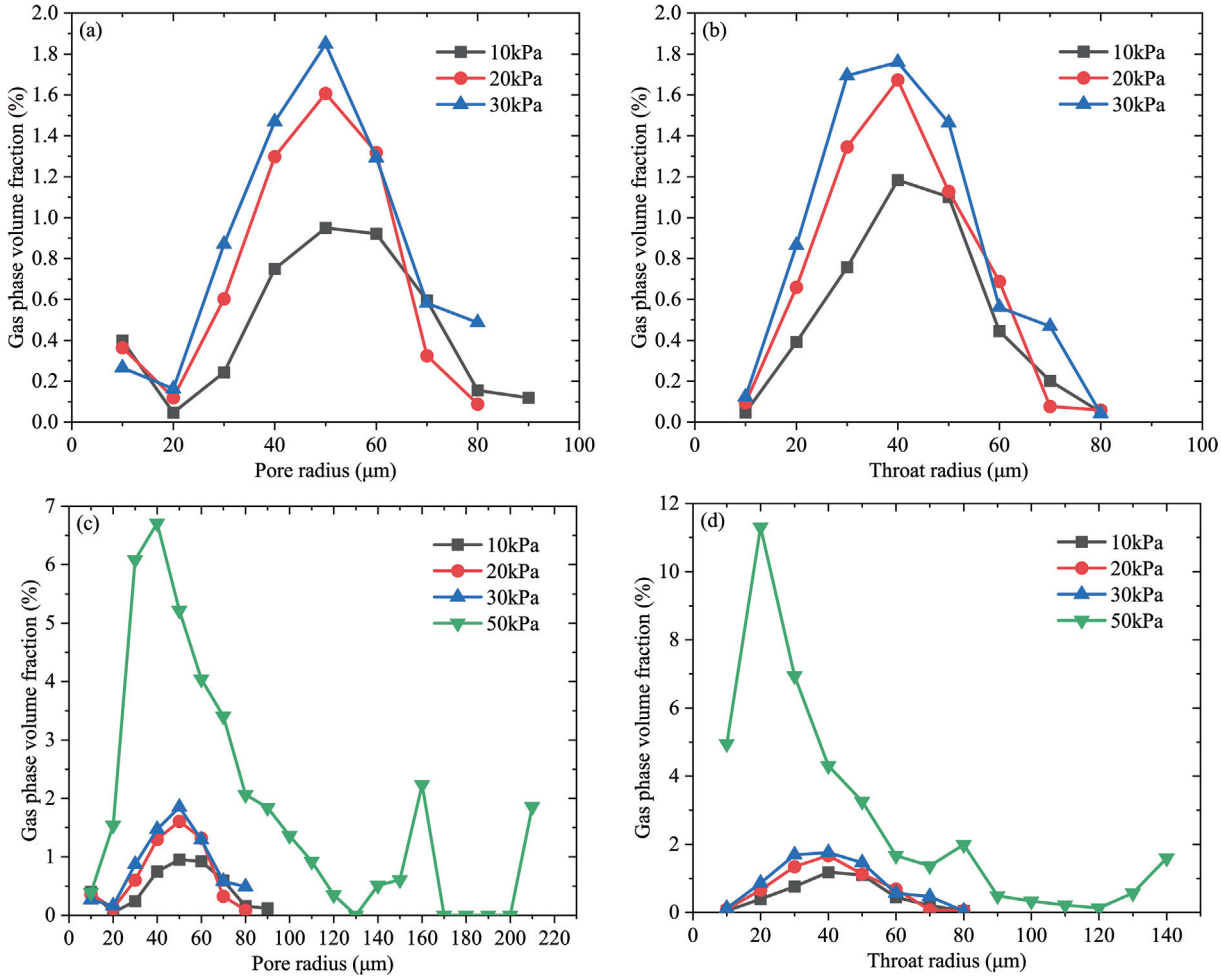

Fig. 15. Pore-throat gas phase volume fraction under different pressures. (a) Pore body gas phase volume fraction for pressures in the range 10–30 kPa, (b) pore throat gas phase volume fraction for 10–30 kPa, (c) pore body gas phase volume fraction for 10–50 kPa, (c) pore throat gas phase volume fraction for 10–50 kPa.

The displacement of water in the pressure range 10–20 kPa is also larger than that for 20–30 kPa, which are 29% and 17% respectively. The 50 kPa and 10–30 kPa gas phase volume fraction changes (Fig. 15c) shows that when the gas pressure reaches 50 kPa, the gas phase pore volume distribution is completely reconstructed. A new peak appears at the peak of 10–30 kPa (about 50 μm), and a series of pores larger than the maximum pore radius (90 μm) at 10–30 kPa also appears with the maximum radius increased to 210 μm. The pore volume for a pressure of 50 kPa increases by 82% compared with that at 30 kPa. The 50 kPa and 10–30 kPa gas phase volume fraction curves (Fig. 15d) show that when the gas pressure reaches 50 kPa, the gas phase volume within the throats is also completely reconstructed. A new peak appears at 20 μm, and a series of throats larger than the maximum pore radius (80 μm) for 10–30 kPa also appears with a maximum radius increased to 140 μm.

4.6. Relationship between quantitative characterization parameters for gas distribution and permeability

Table 3 shows the gas-phase pore-throat structure parameters under different pressures, as calculated from the gas phase volume fraction curve of Fig. 9. The average pore radius, average throat radius and average throat length are positively correlated with the pressure, indicating that the gas seepage space expands with an increase in gas pressure. Except for at 50 kPa, the maximum pore radius, the maximum pore throat radius and the maximum pore throat length have no obvious positive correlation with the pressure - indicating that the pressure does not change the maximum pore and throat volumes of the gas seepage space. As noted above, with the increase of pressure, the water in progressively smaller pores is mainly driven out. The coordination number has a positive correlation with the pressure, indicating that with the increase of the pressure, the connectivity of the pore space increases.

After fitting the pore-throat structure parameters in Table 3 with the gas permeability, it is found that only the average throat length has a significant positive linear correlation with the gas permeability (Fig. 16), indicating that in this experiment, the average throat length is the main factor controlling gas permeability.

Based on the assumption of a fractal geometry, the fractal structure parameters of the gas phase under different pressures are calculated: the fractal dimension characterizes the volume and distribution of the pore space, the lacunarity characterizes the heterogeneity of the gas space and the succolarity characterizes the number of individual connected gas pores (Mandelbrot, 1982; Xia et al., 2019). The fractal dimension has a clear positive correlation with the pressure, indicating that the gas volume both increases and becomes progressively more complex with an increase in pressure. When the gas pressure is increased from 10 to 30 kPa, the increasing lacunarity indicates that the liquid phase around the gas phase space is more easily displaced, gas-filled pore

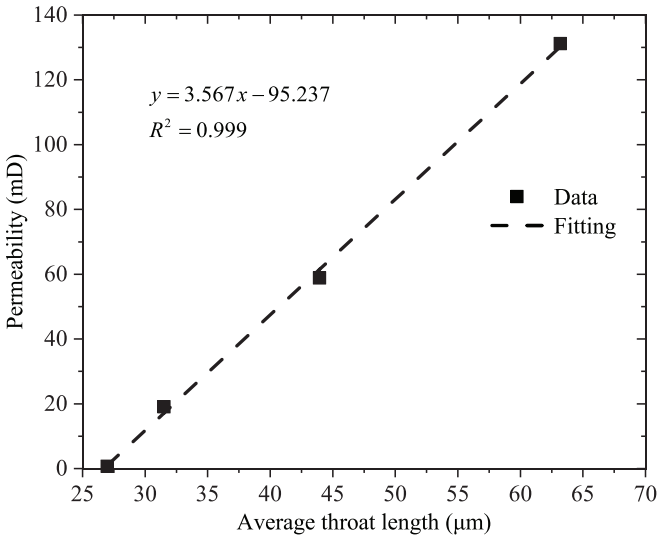

Fig. 16. Permeability versus average pore throat length at different pressures.

space becomes more agglomerated and the heterogeneity increases. Notably, when the pressure reaches 50 kPa, the lacunarity is the smallest, indicating that the reconstructed gas space is evenly distributed throughout the entire sample. The significant increase in the succolarity with increased pressure directly indicates that with the progress of the experiment, the connected gas space in the sample increases significantly.

After fitting the fractal structure parameters (Table 4) with the gas permeability, it is found that the fractal dimension, the succolarity and the gas permeability have a significant positive linear correlation (Fig. 17), indicating that in this experiment, the fractal dimension and the succolarity are the main factors controlling gas permeability. The lack of the correlation between the lacunarity and the gas permeability indicates that the heterogeneity of the gas space of the clayey-silt samples is not the main factor controlling the gas permeability.

Table 4
Fractal structure parameters under different pressures.

Gas displacement pressures (kPa)	Fractal dimension	Lacunarity	Succolarity
10	2.46	0.48	0.0028
20	2.50	0.49	0.0033
30	2.53	0.51	0.0240
50	2.87	0.36	0.0643

5. Conclusions

We explore the evolution of gas permeability within clayey-silt samples from methane hydrate reservoirs in the South China Sea, under varying conditions of gas pressures and saturations and supported by X-ray CT imaging, to provide critical insights into the effects of water–gas distribution on gas seepage characteristics. The findings significantly advance the understanding of gas recovery optimization from such reservoirs:

(1) Enhancement of permeability with gas displacement: A marked increase in flow rate and permeability was observed when gas displacement pressures reached 10, 20, and 30 kPa. Crucially, exceeding the pre-consolidation pressure (30 kPa) not only further amplifies these effects but also stabilizes them at higher pressures, indicating the pivotal role of pre-consolidation pressure in gas recovery efficiency.

(2) Structural transformations in the reservoir: The research highlights that gas displacement initially targets liquid in larger pores, with increased pressure progressively affecting smaller pores. Exceeding pre-consolidation pressure leads to comprehensive liquid displacement, micro-fracture formation and a significant increase in pore volume (~15%), facilitated by a substantial fracture. These transformations are key to enhancing permeability and improving gas extraction rates.

(3) Impact of pore space heterogeneity on permeability: The observed heterogeneity of the pore space distribution significantly influences liquid saturation and thereby gas permeability. Even minor increases in liquid saturation substantially reduce permeability, underscoring the sensitivity of gas permeability to saturation levels and the importance of water management for reservoir permeability enhancement.

(4) Reconstitution of gas-filled porosity: The study shows that with increasing pressure, water is significantly displaced from smaller pore-throats, leading to a complete reconstitution and increase of the gas-filled porosity at 50 kPa. This phenomenon is crucial in enhancing gas flow paths and improving reservoir exploitation strategies.

(5) Determinants of gas permeability: A significant positive linear correlation was found between gas permeability and parameters such as average pore throat length, fractal dimension, and succolarity, highlighting these as the main factors controlling gas permeability. This correlation is essential for the development of predictive models and effective reservoir management.

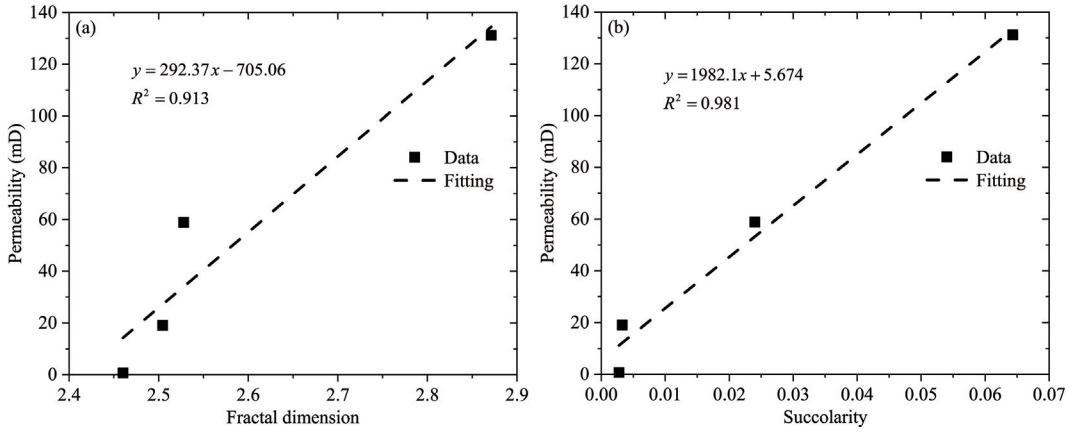

Fig. 17. Permeability versus (a) fractal dimension and (b) succolarity at different pressures.

These insights are instrumental in laying the foundation for improved predictive modeling and offer valuable strategies for the effective development of methane hydrate reservoirs. They emphasize the critical importance of pressure management, micro-structural analysis and saturation control in optimizing gas recovery processes.

CRediT authorship contribution statement

Yuxuan Xia: Conceptualization, Data curation, Formal analysis, Funding acquisition, Investigation, Methodology, Writing – original draft. **Derek Elsworth:** Funding acquisition, Methodology, Validation, Writing – review & editing. **Jianchao Cai:** Funding acquisition, Methodology, Project administration, Supervision, Writing – review & editing. **Cheng Lu:** Funding acquisition, Methodology, Resources, Writing – review & editing. **Chao Ma:** Data curation, Formal analysis.

Declaration of competing interest

The authors declare that they have no known competing financial interests or personal relationships that could have appeared to influence the work reported in this paper.

Acknowledgements

The authors are grateful to the National Natural Science Foundation of China (Nos. 42302143, 42172159, U2244223); China Postdoctoral Science Foundation (No. 2023M743870), China Geological Survey Project (No. DD20211350), and the Science Foundation of China University of Petroleum, Beijing (No. 2462023XKBH002). DE gratefully acknowledges support from the G. Albert Shoemaker endowment.

References

Bian, H., Qin, X., Sun, J., Luo, W., Lu, C., Zhu, J., Ma, C., Zhou, Y., 2023. The impact of mineral compositions on hydrate morphology evolution and phase transition hysteresis in natural clayey silts. Energy 274, 127303.

Blunt, M.J., Bijeljic, B., Dong, H., Gharbi, O., Iglauer, S., Mostaghimi, P., Paluszny, A., Pentland, C., 2013. Pore-scale imaging and modelling. Adv. Water Resour. 51, 197–216.

Boswell, R., Yoneda, J., Waite, W.F., 2019. India National gas Hydrate Program Expedition 02 summary of scientific results: evaluation of natural gas-hydrate-bearing pressure cores. Mar. Petrol. Geol. 108, 143–153.

Cai, J., Xia, Y., Lu, C., Bian, H., Zou, S., 2020a. Creeping microstructure and fractal permeability model of natural gas hydrate reservoir. Mar. Petrol. Geol. 115, 104282.

Cai, J., Xia, Y., Xu, S., Tian, H., 2020b. Advances in multiphase seepage characteristics of natural gas hydrate sediments. Chinese Journal of Theoretical and Applied Mechanics 52 (1), 208–223 (in Chinese with English abstract).

Chen, B., Sun, H., Zheng, J., Yang, M., 2020. New insights on water-gas flow and hydrate decomposition behaviors in natural gas hydrates deposits with various saturations. Appl. Energy 259, 114185.

Chen, X., Verma, R., Espinoza, D.N., Prodanović, M., 2018. Pore-scale determination of gas relative permeability in hydrate-bearing sediments using X-ray computed micro-tomography and lattice boltzmann method. Water Resour. Res. 54 (1), 600–608.

Cui, Y., Lu, C., Wu, M., Peng, Y., Yao, Y., Luo, W., 2018. Review of exploration and production technology of natural gas hydrate. Adv. Geo-Energy Res. 2 (1), 53–62.

Dai, S., Seol, Y., 2014. Water permeability in hydrate-bearing sediments: a pore-scale study. Geophys. Res. Lett. 41 (12), 4176–4184.

Dallimore, S.R., Wright, J.F., Nixon, F.M., Kurihara, M., Yamamoto, K., Fujii, T., Fujii, K., Numasawa, M., Yasuda, M., Imasato, Y., 2008. Geologic and porous media factors affecting the 2007 production response characteristics of the JOGMEC/NRCAN/AURORA Mallik Gas Hydrate Production Research Well. In: Proceedings of the 6th International Conference on Gas Hydrates (ICGH 2008), Vancouver, British Columbia, CANADA, July 6-10, 2008.

Delli, M.L., Grozic, J.L.H., 2014. Experimental determination of permeability of porous media in the presence of gas hydrates. J. Petrol. Sci. Eng. 120, 1–9.

Dong, H., Blunt, M.J., 2009. Pore-network extraction from micro-computerized-tomography images. Phys. Rev. E 80, (3) 036307.

Dong, C., Wang, L., Zhou, Y., Huang, F., Song, Y., Zhou, B., Xu, H., 2020. Microcosmic retaining mechanism and behavior of screen media with highly argillaceous fine sand from natural gas hydrate reservoir. J. Nat. Gas Sci. Eng. 83, 103618.

Esmaeilzadeh, F., Hamedi, N., Karimipourfard, D., Rasoolzadeh, A., 2020. An insight into the role of the association equations of states in gas hydrate modeling: a review. Petrol. Sci. 17 (5), 1432–1450.

Gajanayake, S.M., Gamage, R.P., Li, X.-S., Huppert, H., 2023. Natural gas hydrates – insights into a paradigm-shifting energy resource. Energy Rev. 2, (1) 100013.

Gong, G., Guojun, Z., Pang, W., Yang, M., Chen, B., Zheng, J.-N., 2023. Review of hydrate-bearing sediment permeability for natural gas hydrate exploitation: measurement and application development. J. Petrol. Sci. Eng. 220, 111217.

Katagiri, J., Konno, Y., Yoneda, J., Tenma, N., 2017. Pore-scale modeling of flow in particle packs containing grain-coating and pore-filling hydrates: verification of a kozeny–carman-based permeability reduction model. J. Nat. Gas Sci. Eng. 45, 537–551.

Konno, Y., Jin, Y., Uchiumi, T., Nagao, J., 2013. Multiple-pressure-tapped core holder combined with X-ray computed tomography scanning for gas–water permeability measurements of methane-hydrate-bearing sediments. Rev. Sci. Instrum. 84, (6) 064501.

Li, Y., Liu, L., Jin, Y., Wu, N., 2021. Characterization and development of natural gas hydrate in marine clayey-silt reservoirs: a review and discussion. Adv. Geo-Energy Res. 5 (1), 75–86.

Li, J.-F., Ye, J.-L., Qin, X.-W., Qiu, H.-J., Wu, N.-Y., Lu, H.-L., Xie, W.-W., Lu, J.-A., Peng, F., Xu, Z.-Q., Lu, C., Kuang, Z.-G., Wei, J.-G., Liang, Q.-Y., Lu, H.-F., Kou, B.-B., 2018. The first offshore natural gas hydrate production test in South China Sea. China Geology 1 (1), 5–16.

Liu, H., Yao, Y., Deng, H., 2011. Geological and geophysical conditions for potential natural gas hydrate resources in southern South China Sea waters. J. Earth Sci. 22 (6), 718–725.

Lu, Y., Jin, Y., Li, H., 2023b. Impact of capillary pressure on micro-fracture propagation pressure during hydraulic fracturing in shales: an analytical model. Capillarity 8 (3), 45–52.

Lu, C., Xia, Y., Sun, X., Bian, H., Qiu, H., Lu, H., Luo, W., Cai, J., 2019. Permeability evolution at various pressure gradients in natural gas hydrate reservoir at the shenhu area in the South China Sea. Energies 12 (19), 3688.

Lu, C., Xia, Y., Qin, X., Ma, C., Bian, H., Xing, D., Lu, H., 2022. Micro- and nanoscale pore structure characterization and mineral composition analysis of clayey-silt hydrate reservoir in South China Sea. Geofluids 2022, 2837193.

Lu, C., Qin, X., Sun, J., Wang, R., Cai, J., 2023a. Research progress and scientific challenges in the depressurization exploitation mechanism of clayey-silt natural gas hydrates in the northern South China Sea. Adv. Geo-Energy Res. 10 (1), 14–20.

Makogon, Y.F., Holditch, S.A., Makogon, T.Y., 2007. Natural gas-hydrates — a potential energy source for the 21st century. J. Petrol. Sci. Eng. 56 (1), 14–31.

Mandelbrot, B.B., 1982. The fractal geometry of nature. W. H. Freeman, New York.

Minagawa, H., Nishikawa, Y., Ikeda, I., Miyazaki, K., Takahara, N., Sakamoto, Y., Komai, T., Narita, H., 2008. Characterization of sand sediment by pore size distribution and permeability using proton nuclear magnetic resonance measurement. J. Geophys. Res.-Solid Earth 113 (B7), B07210.

Ning, F., Fang, X., Li, Y., Dou, X., Wang, L., Liu, Z., Luo, Q., Sun, J., Zhao, Y., Zhang, Z., Liu, T., Zhang, L., Jiang, G., 2020. Research status and perspective on wellbore sand production from hydrate reservoirs. Bull Geol. Sci. Technol. 39 (1), 137–148 (in Chinese with English abstract).

Qin, X., Liang, Q., Ye, J., Yang, L., Qiu, H., Xie, W., Liang, J., Lu, J.a., Lu, C., Lu, H., Ma, B., Kuang, Z., Wei, J., Lu, H., Kou, B., 2020. The response of temperature and pressure of hydrate reservoirs in the first gas hydrate production test in South China Sea. Appl. Energy 278, 115649.

Ren, X., Guo, Z., Ning, F., Ma, S., 2020. Permeability of Hydrate-Bearing Sediments. Earth-Sci. Rev. 202, 103100.

Ruppel, C.D., Kessler, J.D., 2017. The interaction of climate change and methane hydrates. Rev. Geophys. 55 (1), 126–168.

Schoderbek, D., Martin, K.L., Howard, J., Silpngarmlert, S., Hester, K., 2012. North slope hydrate fieldtrial: CO_2/CH_4 exchange, OTC Arctic Technology Conference. OTC, pp. OTC-23725-MS.

Shaibu, R., Sambo, C., Guo, B., Dudun, A., 2021. An assessment of methane gas production from natural gas hydrates: challenges, technology and market outlook. Adv. Geo-Energy Res. 5 (3), 318–332.

Sloan, E.D., 2003. Fundamental principles and applications of natural gas hydrates. Nature 426 (6964), 353.

Sun, X., Luo, T., Wang, L., Wang, H., Song, Y., Li, Y., 2019. Numerical simulation of gas recovery from a low-permeability hydrate reservoir by depressurization. Appl. Energy 250, 7–18.

Waite, W.F., Winters, W.J., Mason, D., 2004. Methane hydrate formation in partially water-saturated Ottawa sand. Am. Mineral. 89 (8–9), 1202–1207.

Waite, W.F., Santamarina, J.C., Cortes, D.D., Dugan, B., Espinoza, D.N., Germaine, J., Jang, J., Jung, J.W., Kneafsey, T.J., Shin, H., Soga, K., Winters, W.J., Yun, T.-S., 2009. Physical properties of hydrate-bearing sediments. Rev. Geophys. 47 (4), RG4003.

Wu, N., Huang, L., Hu, G., Li, Y., Chen, Q., Liu, C., 2017. Geological controlling factors and scientific challenges for offshore gas hydrate exploration. Mar. Geol. Quat. Geol. 37 (5), 1–11.

Xia, Y., Cai, J., Perfect, E., Wei, W., Zhang, Q., Meng, Q., 2019. Fractal dimension, lacunarity and succolarity analyses on CT images of reservoir rocks for permeability prediction. J. Hydrol. 579, 124198.

Yamamoto, K., Terao, Y., Fujii, T., Ikawa, T., Seki, M., Matsuzawa, M., Kanno, T., 2014. Operational overview of the first offshore production test of methane hydrates

in the eastern nankai trough, offshore technology conference. OTC, pp. D031S034R004.
Ye, J., Qin, X., Xie, W., Lu, H., Ma, B., Qiu, H., Liang, J., Lu, J.A., Kuang, Z., Lu, C., Liang, Q., Wei, S., Yu, Y., Liu, C., Li, B., Shen, K., Shi, H., Lu, Q., Li, J., Kou, B., Song, G., Li, B., Zhang, H.E., Lu, H., Ma, C., Dong, Y., Bian, H., 2020. Main progress of the second gas hydrate trial production in the South China Sea. Geology in China 47 (03), 557–568 (in Chinese with English abstract).
Yoneda, J., Oshima, M., Kida, M., Kato, A., Konno, Y., Jin, Y., Jang, J., Waite, W.F., Kumar, P., Tenma, N., 2019. Permeability variation and anisotropy of gas hydrate-bearing pressure-core sediments recovered from the krishna-Godavari Basin, offshore India. Mar. Petrol. Geol. 108, 524–536.
Yu, X., Wang, J., Liang, J., Li, S., Zeng, X., Sha, Z., Kuang, Z., Li, W., 2014. Depositional accumulation characteristics of gas hydrate in the northern continental slope of South China Sea. Acta Petrolei Sinica 35 (2), 253–264 (in Chinese with English abstract).
Zhang, L., Dong, H., Dai, S., Kuang, Y., Yang, L., Wang, J., Zhao, J., Song, Y., 2022. Effects of depressurization on gas production and water performance from excess-gas and excess-water methane hydrate accumulations. Chem. Eng. J. 431, 133223.
Zhang, W., Liang, J., Lu, J.a., Wei, J., Su, P., Fang, Y., Guo, Y., Yang, S., Zhang, G., 2017. Accumulation features and mechanisms of high saturation natural gas hydrate in Shenhu Area, northern South China Sea. Petrol. Explor. Dev. 44(5), 708-719.
Zhao, J., Liu, Y., Guo, X., Wei, R., Yu, T., Xu, L., Sun, L., Yang, L., 2020. Gas production behavior from hydrate-bearing fine natural sediments through optimized step-wise depressurization. Appl. Energy 260, 114275.